

Feature Article

**PARSEC – the pseudopotential algorithm
for real-space electronic structure calculations:
recent advances and novel applications to nano-structures****Leeor Kronik^{*,1}, Adi Makmal¹, Murilo L. Tiago^{2,5}, M. M. G. Alemany³, Manish Jain⁴,
Xiangyang Huang^{**,5}, Yousef Saad⁶, and James R. Chelikowsky^{2,5}**¹ Department of Materials and Interfaces, Weizmann Institute of Science, Rehovoth 76100, Israel² Center for Computational Materials, Institute for Computational Engineering and Sciences,
Departments of Physics and Chemical Engineering, University of Texas, Austin, Texas 78712, USA³ Departamento de Física de la Materia Condensada, Facultad de Física,
Universidad de Santiago de Compostela, 15782 Santiago de Compostela, Spain⁴ 3M Company, Corporate Research Materials Laboratory, St. Paul, Minnesota 55144-1000, USA⁵ Department of Chemical Engineering and Materials Science, University of Minnesota, Minneapolis,
Minnesota 55455, USA⁶ Computer Science and Engineering, University of Minnesota, Minneapolis, Minnesota 55455, USA

Received 7 December 2005, revised 20 February 2006, accepted 21 February 2006

Published online 29 March 2006

PACS 61.46.+w, 71.15.Mb, 73.22.-f

We describe the formalism, as well as numerical and implementation issues behind PARSEC – the pseudopotential algorithm for real-space electronic structure calculations. Its current capabilities are illustrated via application of PARSEC to numerous problems in nanoscience.

© 2006 WILEY-VCH Verlag GmbH & Co. KGaA, Weinheim

1 Introduction

A widely used approach to calculating the electronic structure of materials from first principles uses a combination of density functional theory (DFT) [1, 2] and pseudopotential theory [3, 4]. Within DFT, the original n -electron Schrödinger problem is mapped into an effective one-electron problem, where all non-classical electron interactions (namely, exchange and correlation) are subsumed into an additive one-electron potential that is a functional of the charge density. In the pseudopotential approximation, only valence electrons are treated explicitly. Core electrons are suppressed by replacing the true atomic potential with an effective “pseudopotential” that takes the effect of core electrons into account. By combining the two theories we obtain smooth, slow varying potentials and a greatly reduced number of required one-electron wave functions. This significantly facilitates the attainment of converged numerical solutions.

Most currently available codes based on combining these two ideas use the planewave approach [4–8], in which the wave functions of periodic structures are Fourier expanded on a planewave basis. The

* Corresponding author: e-mail: leeor.kronik@weizmann.ac.il

** Current address: R. J. Mears, LLC, 1100 Winter Street, Suite 4700, Waltham, MA 02452, USA

traditional planewave approach has several major disadvantages: First, the planewave approach requires extensive “global” communications and, as such, is not amenable to massive parallelization. Second, for non-periodic systems, e.g., nano-structures, it requires the use of a super-cell, where the aperiodic structure is artificially replicated periodically inside a cell (which is hopefully large enough to avoid spurious structure–replica interaction). This typically increases the cost of the calculation significantly. Third, charged systems require a compensating background charge, which may alter the physical properties of the system.

More than ten years ago, Chelikowsky, Troullier and Saad have suggested that all of these disadvantages may be circumvented if one resorts to a high-order finite difference solution on a real-space grid [9]. This approach has many advantages. Unlike the planewave method, it produces Hamiltonian matrices that are very sparse (although typically larger than those used in planewave calculations). Therefore, the Hamiltonian is never computed or stored explicitly, instead only its action on a wave function vector is computed. It is also much easier to parallelize the computation [10, 11]. Because the computation does not assume periodicity, all other issues raised above are inherently resolved if open boundary conditions are used. Still, it is reasonably simple to implement periodic boundary conditions as well [12].

Over the years, the finite-difference real-space approach has gained in its abilities and has been applied to many physical systems of interest. It has now evolved into a mature, massively parallel software suite, which we call PARSEC – pseudopotential algorithm for real-space electronic structure calculations. The purpose of this article is to describe briefly the current capabilities of PARSEC and to illustrate their application to selected problems in nanoscience. We focus on nano-structures because they provide for very interesting physics – the role confinement (in one or more dimensions) plays in determining chemical, optical, electrical, magnetic, and other properties of matter [13–15]. At the same time, nano-structures are one arena where the relative strengths of the real-space method are easily demonstrated.

The article is arranged as follows. We start with a brief description of the computational approach, including formalism, numerical, and implementation issues. We then highlight various capabilities by reviewing some recent nano-structure applications. These include: open and periodic boundary conditions, demonstrated via size dependence of the electronic structure of nano-crystals and nano-wires, respectively; Spin-polarization, illustrated via studies of nano-crystalline dilute magnetic semiconductors; Langevin Molecular Dynamics, demonstrated via photoemission spectra of Si clusters; Calculations of optical spectra using time-dependent DFT, illustrated on Si and Ge nanocrystals; polarizability calculations and optimized effective potentials, both explained through the electric response of molecular chains.

2 PARSEC principles

Within pseudopotential DFT, we aim to solve the Kohn–Sham [2] Schrödinger-like set of one-particle equations:

$$\left(-\frac{\nabla^2}{2} + V_{\text{ps}}(\mathbf{r}) + V_{\text{H}}(\mathbf{r}) + V_{\text{xc}}[\rho(\mathbf{r})] \right) \varphi_i(\mathbf{r}) = \varepsilon_i \varphi_i(\mathbf{r}), \quad (1)$$

with

$$\rho(\mathbf{r}) = \sum_{i=1}^{\text{occup}} |\varphi_i(\mathbf{r})|^2, \quad (2)$$

where the sum runs over the occupied states. $\varphi_i(\mathbf{r})$ and ε_i are the i -th eigenfunction (single electron wave function) and eigenvalue (energy level), respectively. V_{ps} is the ionic pseudopotential, V_{H} is the Hartree (electron–electron) potential and V_{xc} is the exchange–correlation potential, defined as the functional derivative of the exchange correlation energy with respect to ρ , the charge density: $V_{\text{xc}}(\mathbf{r}) = \frac{\delta E_{\text{xc}}[\rho]}{\delta \rho(\mathbf{r})}$.

Here and in the rest of the text, we use atomic units ($e = m = \hbar = 1$) unless otherwise stated. Equations (1) and (2) are coupled through the charge density. Solving the Kohn–Sham equations is done by iterating to self-consistency.

Within PARSEC, we place a uniform, Cartesian grid in real space, as shown in Fig. 1. We solve Eqs. (1) and (2) for the grid-sampled values of wave functions, potentials, and the electron density. The Kohn–Sham wave functions then become finite-sized vectors and each of the operators in the Kohn–Sham equation (kinetic, pseudopotential, Hartree, and exchange-correlation) is represented by a matrix. Let us briefly describe how each matrix can be constructed.

The “heart” of PARSEC lies in its treatment of the kinetic energy term. It uses a straightforward finite-differencing scheme, but with a *higher-order* expansion for the Laplacian operator. Within this method, the discretization of the Laplacian is done by using *several* neighbors for calculating the derivative around each point, instead of just the immediate neighbors, i.e.:

$$\nabla^2 \varphi(x, y, z) = \frac{1}{h^2} \sum_{k=-M}^M \sum_{l=-M}^M \sum_{m=-M}^M [C_k \varphi(x + kh, y, z) + C_l \varphi(x, y + lh, z) + C_m \varphi(x, y, z + mh)], \quad (3)$$

where M is half the number of neighbors used along each axis, i.e., half the *expansion order*, and h is the grid spacing, i.e., $x_{n+1} - x_n$. The coefficients C_m depend only on the choice of the expansion order, $2M$. Thus, they are found once and for all, regardless of the iterative procedure. They are, in principle, to be found from a high-order Taylor expansion, although other algorithms for their determination are also available [16]. The kinetic energy matrix has only $6M$ elements in each row (in addition to the diagonal), resulting in a very sparse matrix.

Interestingly, Jordan and Mazziotti have demonstrated the use of Eq. (3) within PARSEC with coefficients C_m derived from spectral differences, rather than finite differences [17]. They have shown that this accelerates numerical convergence with respect to grid size without sacrificing the sparsity of the Hamiltonian matrix. This approach is not currently implemented in the distribution version of PARSEC.

The true ionic potential is fully local and is given by $V_{\text{ion}}(\mathbf{r}) = -\sum_{a=1}^N \frac{Z_a}{|\mathbf{R}_a - \mathbf{r}|}$, where Z_a and \mathbf{R}_a are the atomic number and position of atom a , respectively, and N is the number of atoms in the system. However, this seemingly simple form of the ionic potential causes serious numerical problems: First, it is singular at the atomic sites. Second, it results in single electron wave functions that oscillate rapidly near the nuclei, demanding an unrealistically large number of grid points. Within pseudopotential theory, both problems are circumvented. Furthermore, the number of electrons for which the system has to be solved is reduced significantly because core electrons are taken into account only implicitly. There are many

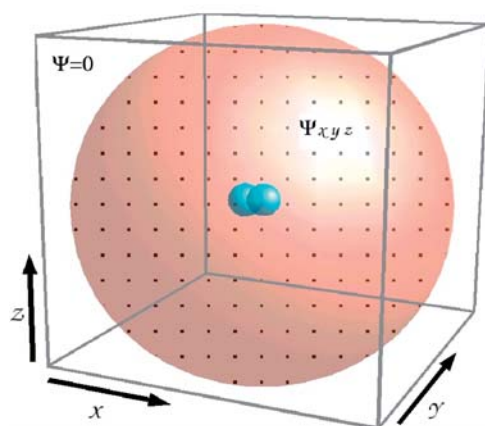


Fig. 1 An illustration of the finite-difference real space approach. For open boundary conditions (shown in the figure), wave functions are sampled on a 3D uniform grid within a spherical domain and vanish outside its boundary. Black dots denote grid points and the blue balls denote atoms (a dimer example is shown).

algorithms for constructing reliable pseudopotentials [3, 4, 11]. PARSEC uses norm conserving pseudopotentials. Typically Troullier–Martins pseudopotentials [18] are used. These potentials have been optimized for convergence with a plane wave basis, can be easily implemented within a real space method, and in our experience are as useful in real space as they are with planewaves. However, any other norm-conserving pseudopotential is also compatible with PARSEC.

The price to be paid for the great simplification afforded by pseudopotentials is that the ionic potential operator is no longer local. This is because different atomic orbitals have different pseudopotentials, so that application of the pseudopotential requires non-local projectors, i.e. [11]:

$$V_{\text{ps}}(\mathbf{r}) = \sum_{a=1}^N \sum_l V_{a,\text{ps}}^l(|\mathbf{r} - \mathbf{R}_a|) \sum_{m=-l}^l |l, m\rangle \langle l, m|, \quad (4)$$

where $V_{a,\text{ps}}^l$ is the pseudopotential of the l -th angular momentum orbital of the a -th atom, \mathbf{R}_a is the coordinate of the a -th atom, and $|l, m\rangle$ is the lm -th spherical harmonic. One relatively easy way of making the matrix corresponding to the pseudopotential operator sparse is not to use Eq. (4) as is, but instead to use the projection scheme suggested by Kleinman and Bylander [19]:

$$V_{\text{ps}}(\mathbf{r}) = \sum_{a=1}^N \left[V_{a,\text{ps}}^{\text{loc}}(\mathbf{r}) + \frac{|\Delta V_{a,\text{ps}}^l(\mathbf{r}) \phi_{lm}^a(\mathbf{r})\rangle \langle \Delta V_{a,\text{ps}}^l(\mathbf{r}) \phi_{lm}^a(\mathbf{r})|}{\langle \phi_{lm}^a(\mathbf{r}) | \Delta V_{a,\text{ps}}^l(\mathbf{r}) | \phi_{lm}^a(\mathbf{r})\rangle} \right], \quad (5)$$

where $V_{a,\text{ps}}^{\text{loc}}(\mathbf{r})$ is a pseudopotential corresponding to one specific angular momentum component (of atom a), arbitrarily chosen as the local one, and $\Delta V_{a,\text{ps}}^l(\mathbf{r}) \equiv V_{a,\text{ps}}^l(\mathbf{r}) - V_{a,\text{ps}}^{\text{loc}}(\mathbf{r})$. Finally, $\phi_{lm}^a(\mathbf{r})$ is the atomic pseudo wave function with lm quantum angular momentum numbers. This form of the pseudopotential has several advantages: First, $\Delta V_{a,\text{ps}}^l$ differs from zero only inside a relatively small region around each atom (which corresponds to the pseudopotential cutoff radius – see Ref. [11] for a more detailed discussion). Second, only the normalization scalars $c_{lm}^a = \langle \phi_{lm}^a(\mathbf{r}) | \Delta V_{a,\text{ps}}^l(\mathbf{r}) | \phi_{lm}^a(\mathbf{r})\rangle$ and the highly sparse vectors $\mathbf{u}_{lm}^a = |\Delta V_{a,\text{ps}}^l(\mathbf{r}) \phi_{lm}^a(\mathbf{r})\rangle$ are stored explicitly instead of holding an entire matrix. Last, the c_{lm}^a and \mathbf{u}_{lm}^a terms are computed only once in the entire self-consistent solution, because they only depend on the atom coordinates, \mathbf{R}_a , and angular momentum numbers, $\{l, m\}$, which do not change during the iterative computation.

The Hartree potential, given by $V_H(\mathbf{r}) = \int \frac{\rho(\mathbf{r}')}{|\mathbf{r} - \mathbf{r}'|} d\mathbf{r}'$, is not directly evaluated. Instead, it is much more efficient computationally to solve the Poisson equation, $\nabla^2 V_H(\mathbf{r}) = -4\pi\rho(\mathbf{r})$, using the conjugated gradients method [20] (a detailed discussion of the implementation of boundary conditions can be found in Ref. [22]). The Hartree potential is local and therefore its associated matrix must be strictly diagonal. Finally, the exchange-correlation potential is defined as the functional derivative of the exchange-correlation energy with respect to the charge density. Its exact formula depends on the approximate functional used. PARSEC currently supports the Ceperly–Alder form [23] of the local density approximation (LDA) and the Perdew–Burke–Ernzerhof form [24] of the generalized gradient approximation (GGA), as well as the van Leeuwen and Barends [25] and the Casida and Salahub [26] asymptotically corrected functionals (but see below for recent exact exchange work within PARSEC). Irrespectively of the functional, the exchange-correlation potential must be, by definition, a local one [27]. Accordingly, its associated matrix is also diagonal.

The resulting Hamiltonian matrix, being a sum of all matrix operators, each of which is diagonal or highly sparse, is clearly highly sparse itself. The only quantities computed and stored explicitly are the diagonal elements (diagonal component of kinetic energy, local pseudopotential, Hartree potential, and exchange-correlation potential), the high-order finite-difference expansion coefficients, and the relatively small non-local pseudopotential vectors \mathbf{u}_{lm} . This results in huge memory savings, which are crucial for the computation of large systems containing many hundreds of atoms or more, as in some of the examples below.

Given a Hamiltonian, PARSEC calculates a user-prescribed number of the lowest Kohn–Sham eigenvalues and associated eigenfunctions, using iterative diagonalization schemes. At present, two such methods are implemented in the code – one is a generalized Davidson solver written specifically for PARSEC [11, 28]. The other is an Arnoldi algorithm as implemented in the ARPACK code [29]. A detailed discussion of the numerical linear algebra behind these approaches is well outside the scope of the present text. However, an important salient feature in both algorithms is that they obtain solutions using repeated application of the Hamiltonian matrix to guess vectors. It is precisely this property that allows us to avoid an explicit construction of the Hamiltonian, as one only needs to know how it operates on a given vector.

Once the eigenvalues and eigenfunctions are found, the ground state charge density is calculated according to Eq. (2). The new density-dependent terms in the Hamiltonian operator are then constructed by mixing those obtained from the resulting charge density with one or more of the previous ones. At present we find that a generalized Broyden approach [31] provides for effective mixing. The entire process continues until self-consistency of the potentials is achieved, i.e., until the norm of the difference between potentials obtained from consecutive cycles is smaller than a user-prescribed value that is deemed sufficient physically.

PARSEC can be used in either a serial or a parallel mode. Its parallel mode uses MPI (Message Passing Interface) – a standard parallel communications interface. It has been run successfully on as many as 256 processors simultaneously. Parallelization is achieved by domain decomposition, namely, a partitioning of physical space into D sub-domains, where D is the number of processors. In other words, all vectors whose dimension is the number of grid points are partitioned equally between processors according to a spatial mapping. Within this scheme, most of the required numerical operations, i.e., linear combinations of vectors, vector–vector products, and matrix–vector products, are extremely well parallelized. This is because the sparse structure of the matrices requires relatively little inter-processor communication.

A new feature in PARSEC is the use of symmetry. It is always important to explore symmetry operations present in the system at hand and often useful to employ them for simplifying the calculation [30]. In the context of a real-space code such as PARSEC, point symmetries in the position of atoms are explored in a very natural way: the region of space sampled is reduced to an “irreducible wedge”, and existing symmetry operations are then used to unfold wave functions to the full space when needed. For illustrative purposes, we take the example of a confined system with mirror symmetry on the xy -plane. Here, wave functions are either even or odd with respect to reflection through the mirror plane, depending on whether they remain unchanged or gain a phase $e^{i\pi}$ upon the transformation $z \rightarrow -z$. In addition, the Hamiltonian H preserves this symmetry, so that the function $\psi = H\varphi$ is odd (even) upon reflection if φ is odd (even). One can therefore solve the eigenvalue problem given in Eq. (1) using only the $z > 0$ region of space and imposing appropriate boundary conditions: for odd-paired functions, $\varphi = 0$ at $z = 0$; for even-paired functions, $d\varphi/dz = 0$ at $z = 0$. Although the original eigenvalue problem is replaced by two eigenvalue problems with different boundary conditions, the overall numerical load is considerably reduced because the new eigenvalue problems are much simpler [32].

In the above example, the irreducible wedge is the $z > 0$ hemisphere and wave functions are classified as belonging to one of the two irreducible representations of the C_s point group. In the general case, mirror symmetries and 2-fold rotation symmetries are used to construct a point group and the corresponding irreducible wedge in a similar way. Currently, we use only Abelian groups with non-complex characters and therefore some symmetry operations are not explored (e.g., 3-fold rotations). Once the point group is known, Eq. (1) is solved for each one of its irreducible representations. Boundary conditions are defined by the characters of each representation. This scheme has two major advantages. First, the numerical effort spent in solving Eq. (1) is drastically reduced without adding complexity to the code. The same algorithms that handle diagonalizations in the full real-space grid are employed for the irreducible wedge. Parallelization is achieved by distributing the irreducible wedge in sub-domains and using parallelized eigensolvers as before. Second, because the region of space actually sampled is smaller, CPU memory management is also more efficient. Typically, the reduction in CPU memory scales linearly with the number of symmetry operations.

Because the real-space grid implemented in PARSEC is Cartesian, symmetry operations not compatible with a Cartesian, orthogonal grid are currently ignored. This certainly restricts the number of useful symmetry operations, but the inclusion of ignored operations would not improve numerical performance significantly. As an extreme situation, we take the example of the C_{60} fullerene. The point group of this molecule is a subgroup of the icosahedral point group, I_h , which has 10 irreducible representations. This means that the full Hamiltonian can be written as a block-diagonal matrix with up to 10 blocks. For this system, the largest subgroup compatible with the real-space grid is D_{2h} , with 8 irreducible representations. We conclude that despite not handling the full group, PARSEC is still able to utilize 8 out of a maximum of 10 irreducible representations.

Finally, we note that PARSEC is a modern FORTRAN 90/95 code. It was tested and used successfully on a large variety of different platforms, from personal computers, through small work-stations, to large computer clusters and supercomputers.

3 Applications

3.1 Open boundary conditions: nanocrystalline quantum dots

As mentioned above, an important advantage of PARSEC is that it allows for a natural imposition of open boundary conditions (i.e., null wavefunctions outside a sufficiently large domain), making PARSEC attractive for applications to confined systems in general and nano-structures in particular. We demonstrate the benefits of this approach by considering the size evolution of the electronic structure of nanocrystalline quantum dots. Such dots are defined as close-to-spherical passivated fragments of the bulk material, preserving the local crystalline order, with a typical diameter in the nanometer range.

Here, we show an example of Ga_nAs_n nanocrystals of various sizes, ranging from $n = 2$ to $n = 65$. In all cases, the nanocrystal surface is passivated by pseudo-hydrogen atoms [33], so that we can eliminate surface effects. For the largest, $n = 65$ system, if one includes the passivating pseudo-hydrogen atoms a total of 228 atoms with 618 valence electrons are handled. Figure 2 shows both occupied and unoccupied energy levels for several choices of n . All diagrams were aligned such that the highest occupied molecular orbital (HOMO) state was defined as the zero of energy. As expected from basic considerations [14], an inverse correlation between the nanocrystal size and the computed HOMO–lowest unoccupied molecular orbital (LUMO) gap is found [34].

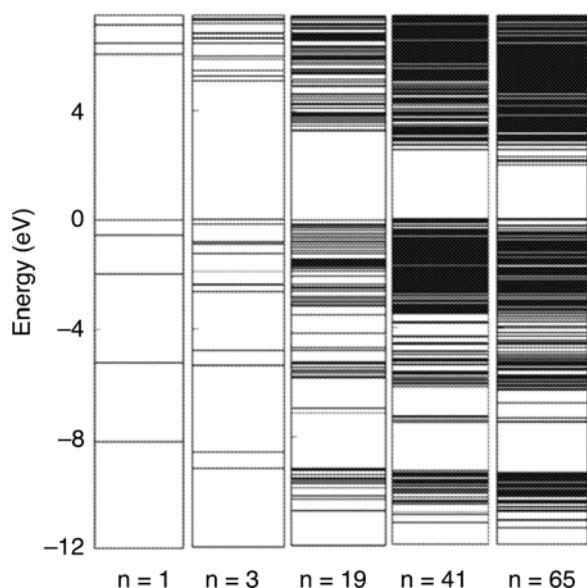


Fig. 2 Energy level diagram for Ga_nAs_n nanocrystals with $n = 2$ to $n = 65$. The HOMO energy level has been set to zero in all diagrams.

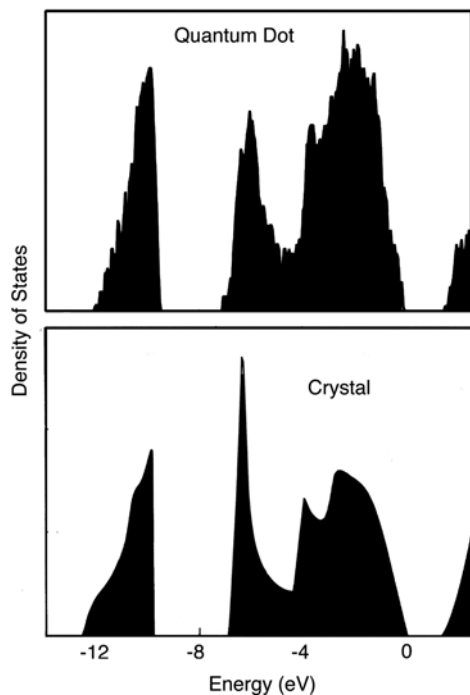


Fig. 3 LDA-computed density of state curve for a $\text{Ga}_{171}\text{As}_{171}$ nanocrystal (top), versus that of bulk GaAs (bottom). The nanocrystal curve was obtained by projecting out the contribution of pseudo-hydrogens, followed by broadening of an energy level diagram similar to those shown in Fig. 2. The bulk curve was computed using empirical pseudopotentials.

Interesting information as to the gradual evolution of the electronic structure towards the bulk limit is obtained from a comparison of the electronic structure of an even larger $\text{Ga}_{171}\text{As}_{171}$ nanocrystal to the density of states (DOS) of the GaAs bulk (computed using empirical pseudopotentials [35]), as shown in Fig. 3. In order to facilitate the comparison, the discrete energy levels of the nanocrystal have been broadened by convolution with a Gaussian, and states corresponding to the surface pseudo-hydrogen atoms were projected out. Clearly, the correspondence between the nanocrystal and bulk DOS is quite good, indicating a rapid convergence of the valence electronic structure to its bulk distribution. It should be noted, however, that the agreement in the forbidden gap value is fortuitous: An underestimate of experiment gaps is a well-known deficiency of time-independent DFT [36] and in this case the underestimated value for the nanocrystal happens to be close to the correct bulk value of the gap.

3.2 Periodic boundary conditions: nano wires

Using open boundary conditions would not be advantageous when attempting to study quantum size effects in nano-wires, i.e., fragments of the bulk that are confined to the nanometer scale in two-dimensions, but quasi-infinite in the third. In this case, it is much easier to use periodic boundary conditions, leaving a sufficient region of vacuum around the bulk fragment in two dimensions as in the nanocrystalline dot, but maintaining periodicity in the third dimension. Periodic boundary conditions have recently been implemented in PARSEC [12]. The main problem associated with periodic boundary conditions is that, taken individually, the local ionic potential, the Hartree potential, and the ion–ion energy term all diverge [37]. Here, this problem is avoided by initially obtaining the contribution to the local ionic pseudopotential in reciprocal space, and then transferring it to the real-space grid by Fourier transform [12]. This does not degrade performance at all because the ionic potential does not change during the self-consistent iterations. Therefore, only one fast Fourier transform (FFT) step and one inverse FFT step are performed in the entire self-consistent calculation, at a negligible computational cost. The self-consistent iterations are performed strictly in real space throughout, as above. Divergence in the Hartree term is avoided even more simply, by first setting the total electronic charge in the supercell to zero be

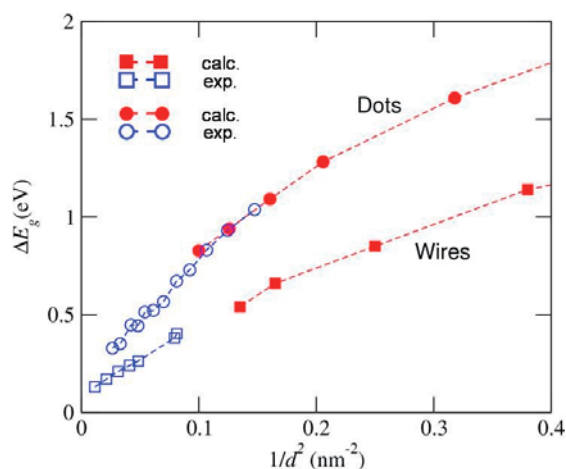


Fig. 4 Difference between the LDA-computed nanosystem gap and bulk gap, as a function of the inverse square radius, for InP nanowires (squares) and nanocrystals (circles). Red: computed values. Blue: experimental values [38].

fore solving the Poisson equation for the Hartree potential. This merely shifts the solution by a known constant. Finally, the ion–ion energy term is also handled via FFT.

PARSEC's ability to use both open and periodic boundary conditions is demonstrated here by comparing the evolution of the HOMO–LUMO gap as a function of radius in InP nanowires and nanocrystals, as shown in Fig. 4. Pseudo-hydrogens were used in both cases as before. In Fig. 4, the difference between the LDA-computed nanosystem gap and bulk gap is plotted as a function of the inverse square radius and is compared to experiment. As expected, the gap in the nanocrystal increases more rapidly with decreasing dot size due to the extra confinement. More strikingly, for both nanowire and nanocrystal an excellent agreement with experiment is obtained.

3.3 Spin polarization: nano crystalline dilute magnetic semiconductors

For handling spin-polarized systems, a generalization of the Kohn–Sham Eqs. (1), (2) presented in Section 2 is required. Such a generalization, usually referred to as spin-polarized DFT, is indeed available [39, 40]. Briefly, it consists of obtaining two separate Kohn–Sham equations, one for each spin channel, that are coupled through an exchange–correlation term that depends on both the spin-up density and the spin-down density, in the form

$$\left(-\frac{\nabla^2}{2} + V_{\text{ion}}(\mathbf{r}) + V_H(\mathbf{r}) + V_{xc,\sigma}[\rho_{\uparrow}(\mathbf{r}), \rho_{\downarrow}(\mathbf{r})] \right) \varphi_{i,\sigma}(\mathbf{r}) = \varepsilon_{i,\sigma} \varphi_{i,\sigma}(\mathbf{r}), \quad \sigma \in \{\uparrow, \downarrow\}, \quad (6)$$

with

$$\rho_{\sigma}(\mathbf{r}) = \sum_{i=1}^{\text{occup}} |\varphi_{i,\sigma}(\mathbf{r})|^2. \quad (7)$$

The availability of spin-polarized calculations in PARSEC makes it immediately attractive for studies of the *magnetic* properties of dilute magnetic semiconducting nanocrystals. This is an important issue, because quantum confinement may play a significant role in shaping the spin-polarized electronic structure of dilute magnetic semiconductors and therefore have intriguing magnetic consequences [13, 42].

In the example shown here, we investigated the electronic structure and magnetic properties of Mn-doped Ge, GaAs, and ZnSe nanocrystals. Because previous experiments have suggested that each nanocrystal contains, on average, one Mn atom [43], we chose to study the effects of placing one or two Mn atoms inside the nanocrystals. We considered four Mn-doped nanocrystals: $X_9\text{MnY}_{10}$, $X_{18}\text{MnY}_{19}$, $X_{40}\text{MnY}_{41}$, and $X_{64}\text{MnY}_{65}$, where $X = \text{Ge, Ga, or Zn}$ and $Y = \text{Ge, As, or Se}$, respectively. The passivating H atoms are implicit. We additionally examined Mn–Mn interactions by considering two Mn atoms that were placed such that they were bridged by an anion atom.

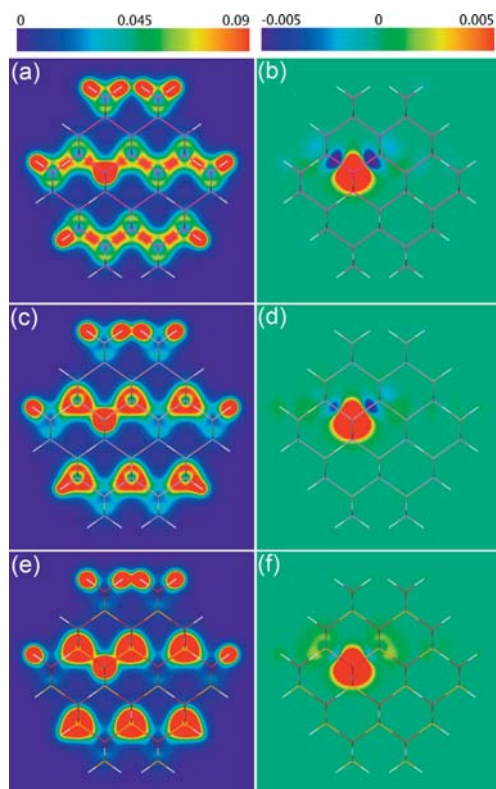


Fig. 5 Total valence charge density (a), (c), (e) and spin density (b), (d), (f) for passivated Ge_{81}Mn , $\text{Ga}_{40}\text{MnAs}_{41}$, and $\text{Zn}_{40}\text{MnSe}_{40}$ nanocrystals, respectively (after Huang et al., Ref. [41]).

Figure 5 shows the total valence charge density ($\rho_{\uparrow} + \rho_{\downarrow}$) and spin-density ($\rho_{\uparrow} - \rho_{\downarrow}$) contour plots obtained for the $\text{X}_{40}\text{MnY}_{41}$ nanocrystals containing one Mn atom. In all cases, the charge density maps show Mn bonding with its nearest neighbors, indicating hybridization between Mn d and anion s–p states. The spin-density maps indicate a strongly localized magnetic moment at the Mn site. Interestingly, for the Ge and GaAs nanocrystals, the spin polarization of the atoms nearest to the Mn atom has an opposite sign to that of Mn, indicating anti-ferromagnetic coupling between the Mn atom and its surroundings.

Figure 6 shows the spin-polarized energy levels for the same systems. Clearly, the presence of Mn introduces gap states inside the otherwise forbidden gap. These levels are well within the host gap, which implies a strong localization of the associated orbitals. Their energy position was found to be relatively insensitive to the size of the nanocrystal because the role of confinement is diminished for a state that is already strongly localized. Consequently, the delocalized occupied orbitals are “pushed down” in energy far more significantly than the Mn states with decreasing nanocrystal size. For, e.g., GaAs, this makes the Mn atom a deep acceptor in the nanocrystal, whereas it is a shallow acceptor in the bulk [44].

This change in the nature of the Mn impurity level has novel consequences for the magnetic interaction between two Mn atoms. By placing two Mn atoms on adjacent cation sites, bridged through an anion, we found the ferromagnetic configuration to be more stable than the antiferromagnetic one in Ge and GaAs, but less stable for ZnSe. This is in agreement with bulk results, but for a different reason: In bulk Ge and GaAs, ferromagnetic Mn–Mn interaction is ascribed to mediation via free carriers [45, 46]. However, Fig. 6 clearly shows the absence of free carriers and thus rules out this mechanism for the nanocrystals. Instead, the ferromagnetic interaction is mediated via localized holes coupled antiferromagnetically to the Mn atoms, a mechanism known as double-exchange. This is also consistent with the lack of ferromagnetic coupling in ZnSe, as there are no available localized holes if the Mn atom replaces a Zn one. This constitutes a novel quantum confinement effect – the influence of size on magnetic coupling mechanisms.

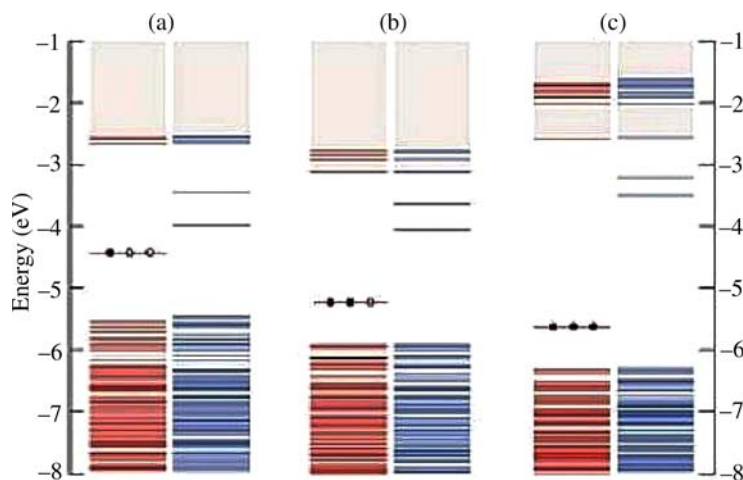


Fig. 6 Spin-polarized electronic structure for passivated (a) Ge_{81}Mn , (b) $\text{Ga}_{40}\text{MnAs}_{41}$, and (c) $\text{Zn}_{40}\text{MnSe}_{41}$ nanocrystals. Filled and empty circles denote electrons and holes, respectively. The majority levels are shown in red (after Huang et al., Ref. [41]).

3.4 Molecular dynamics: parameter-free line shapes of photoelectron spectra

Another useful feature of PARSEC is the ability to perform Born–Oppenheimer molecular dynamics [47, 48]. This is achieved by considering simple Newtonian motion for micro-canonical ensembles and by using the Langevin equation [49] for canonical ensembles, in the form

$$m_a \ddot{\mathbf{R}}_a = \mathbf{F}_a - \beta \dot{\mathbf{R}}_a m_a + \mathbf{G}_a, \quad (8)$$

where \mathbf{R}_a is the position of the a -th atom, \mathbf{F}_a is the force acting on the a -th atom (due to the electrons and other nuclei), m_a is its nuclear mass, β is a viscosity parameter which determines the dissipation rate, and \mathbf{G}_a is “white noise” (Gaussian) stochastic force, such that

$$\langle \mathbf{G}_a^{R_i}(t) \rangle = 0, \quad \langle \mathbf{G}_a^{R_i}(t) \mathbf{G}_b^{R_j}(t') \rangle = 2\beta m_a k_B T \delta_{ab} \delta(t - t'), \quad (9)$$

with T being the temperature in the system and k_B being Boltzmann’s constant.

One application of Langevin molecular dynamics which has found numerous uses with PARSEC is the determination of stable isomers of various clusters using the simulated annealing approach (see, e.g., Refs. [50–52], and references therein). In this approach, the system is virtually “heated up” to a very high temperature and then allowed to cool (relatively) slowly to its stable state. Trapping in local minima is avoided by exploiting the random, “white noise”, force mentioned above, during the search for global minima. In a different recent application, molecular dynamics have been used in conjunction with periodic boundary conditions in order to determine the radial distribution function and static structure factor of liquid silicon, as well as the self-diffusion coefficient [12].

Here, we illustrate the importance of molecular dynamics via yet another capability they afford: the parameter-free simulation of photoemission spectra from the electronic density of states [53–55]. Photoemission spectra are an important source of information for indirect verification of suggested cluster isomers, by comparing computed and measured spectra. However, experimental spectra are usually significantly broader than the computed density of states curves, due to temperature effects. Worse, depending on the pertinent potential energy surfaces, this broadening may be poorly reproduced by standard Gaussian or Lorentzian broadening functions [53, 54]. Isothermal Langevin molecular dynamics affords a natural means for obtaining this broadening without recourse to artificial broadening functions, simply by sampling a large set of structures at a given temperature and averaging over their density of states curves.

Recently, this approach has been applied for testing various isomers of Si anion cluster isomers at the intermediate size range (20 to 26 atoms) [55]. For this size range, isomer identification via simulated annealing is very difficult due to the explosive growth in the number of plausible structures with increasing cluster size. Instead, candidate minimum energy structures were identified via an extensive search algorithm dubbed “big bang” [56], where candidate structures are created by placing atoms randomly within an initial, very small volume and performing a gradient-based relaxation to a local minimum. The energy ranking of the minima is then refined in a hierarchical process of increasing computational sophistication, that results in the lowest 20 or so neutral isomers being fully relaxed within DFT.

As an illustration, low energy isomers of Si_{26}^- are shown in Fig. 7, with associated photoemission spectra shown in Fig. 8. For comparison, experimental PES data [57] are also included in Fig. 8 as the bottom trace. Aside from the molecular-dynamics-driven broadening explained above, the obtained spectra were also shifted such that the highest energy feature coincided with the *computed* vertical detachment energy (VDE – the energy needed to remove an electron from the highest occupied orbital, without relaxing the rest of the system). This allows an *ab initio* placement of the leading peak of the spectrum without introducing an empirical shift of the data. Finally, the spectra were convoluted with a relatively narrow Gaussian function to suppress statistical fluctuations that are below the experimental resolution.

For the four $n = 26$ isomers shown in Fig. 7, isomer (A) is composed of one ten-atom sub-unit and one nine-atom tricapped trigonal prism sub-unit, connected by a seven-atom bridging unit. Isomer (B) is composed of two ten-atom subunits connected by a six-atom bridging unit. Isomers (C) and (D) are both compact structures, but structure (D) is somewhat more prolate while (C) is oblate. Figure 8 shows that isomer (A) yields the best agreement with experiment, in terms of the position of the first two peaks as well as the overall line shape. Isomer (B), which bears some structural similarity to (A), also produces a reasonable spectrum, but the energy of the first two peaks is shifted and the inter-peak separation is larger.

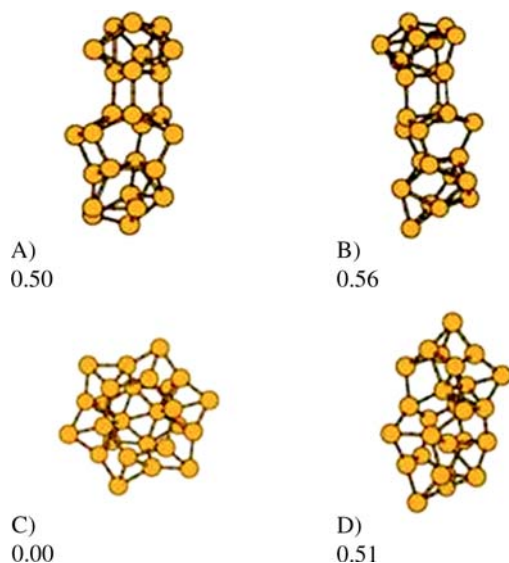


Fig. 7 Selected low-energy isomers for Si_{26}^- . The energy of each structure relative to the respective lowest energy isomer found, in eV, is also given (after Guliamov et al., Ref. [55]).

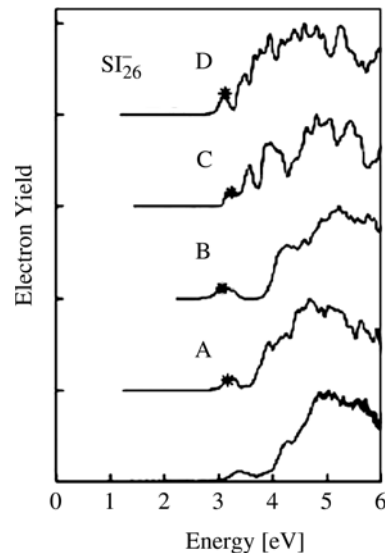


Fig. 8 Comparison of simulated PES data for structures from Fig. 7 with the corresponding experimental PES data (taken from Ref. [57]), for Si_{26}^- . The bottom trace corresponds to the experimental data. In the simulated PES data, the asterisks mark the position of the VDE (after Guliamov et al., Ref. [55]).

The spectrum of isomer (C) also shares some features with the experimental data, namely the position of the leading peak, and the position of the major peak near 5 eV. However, there is an added feature in the theoretical spectrum near 3.6 eV that is not found in the observed data. The spectra of isomer (D) is in markedly worse agreement with experiment than any of the other structures. In terms of energy, the compact structure (C) is the most stable. Interestingly, isomer (A), which appears to yield a spectrum closest to experiment, lies 0.5 eV above the ground state one. This may indicate that there's an isomer lower yet in energy, which has not been found, that yields a similar spectrum. It may also indicate an incorrect energy ordering of the GGA calculation or that kinetic limitations in the experiment dictate the observed isomer.

The above comparison between the predicted and measured PES data, enabled by using Langevin molecular dynamics, indicates that PES can distinguish between structurally distinct isomers at a given cluster size, even for the intermediate size range, where the structural sensitivity is far from obvious.

3.5 Time-dependent DFT applied to nanocrystals of Si and Ge

A major limitation of the original Kohn–Sham formulation of DFT is that it is *inherently* unsuitable for the computation of excited state properties [58]. This is because the Kohn–Sham equations are a reformulation of the time-independent Schrödinger equation that is only suitable for the calculation of ground state properties. Over twenty years ago, Runge and Gross have shown that the time-dependent Schrödinger equation can be mapped to a time-dependent Kohn–Sham equation. This paved the way to time-dependent DFT (TDDFT), which, in principle, can be applied towards the computation to any excited state property, if an exchange-correlation energy that is a functional of the charge density in both time and space is given [59].

In particular, TDDFT can be applied to computation of optical excitation spectra. Fortunately, for many systems (but not all [60]) it has been found that use of the simplest reasonable functional possible – one that depends *locally* on the charge density in both space and time, yields very good agreement with experiment for a wide range of molecules, clusters, and nanocrystals [36].

Compared to other *ab initio* methods for computing excited states in general and optical spectra in particular, TDDFT requires a substantially smaller computational effort and can handle a greater number of atoms. Nevertheless, optical properties of relatively large systems, in the range of many hundreds of atoms, are usually hard to address even within TDDFT.

PARSEC offers an effective way for computing optical excitation spectra, based on a formalism that circumvents explicit propagation of wave functions in time. This is achieved by determining optical transition energies and oscillator strengths from the poles and residues, respectively, of the dynamic polarizability [61]. In this approach, the Kohn–Sham eigenvalues and eigenfunctions are used to construct a new eigenvalue problem, in the form:

$$\left[\omega_{ij\sigma}^2 \delta_{ik} \delta_{jl} \delta_{\sigma\tau} + 2\sqrt{f_{ij\sigma} \omega_{ij\sigma}} K_{ij\sigma,kl\tau} \sqrt{f_{kl\tau} \omega_{kl\tau}} \right] F_n = \Omega_n^2 F_n, \quad (10)$$

where Ω_n are the optical excitation energies, $\omega_{ij\sigma} = \varepsilon_{j\sigma} - \varepsilon_{i\sigma}$ are the Kohn–Sham transition energies, and $f_{ij\sigma} = n_{i\sigma} - n_{j\sigma}$ are the differences between the occupation numbers of the i -th and j -th states. The eigenvectors F_n are related to the oscillator strength, and $K_{ij\sigma,kl\tau}$ is a coupling matrix given by

$$K = \iint \varphi_{i\sigma}(r) \varphi_{j\sigma}(r) \left(\frac{1}{|r-r'|} + \frac{\delta^2 E_{xc}[\rho]}{\delta \rho_\sigma(r) \delta \rho_\tau(r')} \right) \varphi_{k\tau}(r') \varphi_{l\tau}(r') dr dr', \quad (11)$$

where $\varphi(r)$ are the one-electron Kohn–Sham orbitals (see Eq. (1)), and the indices i, j, σ (as well as k, l, τ) indicate for occupied states, unoccupied states and spin, respectively. Practically, one first runs PARSEC to obtain the converged Kohn–Sham eigenvalues and eigenfunctions. Then, using a compatible “TDDFT” package, the coupling matrix is first evaluated in real-space and then used to solve Eq. (10),

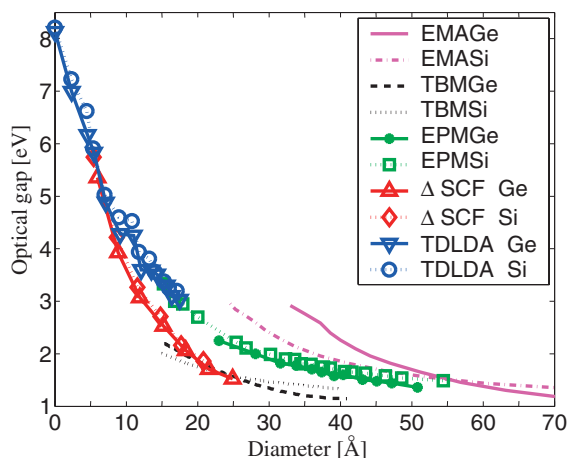


Fig. 9 Optical gap of Ge and Si nanocrystals as a function of diameter, computed using: 1) TDDFT [62], in blue. Down triangles with solid line: Ge; open circles with dotted line: Si. 2) Effective mass approximation [64], in magenta. Solid line: Ge; dash-dotted line: Si. 3) Tight binding [65], in black. Dashed line: Ge; dotted line: Si. 4) Empirical pseudopotentials [66], in green. Solid circles with solid line: Ge; open squares with dotted line: Si. 5) Δ SCF [67], in red. Up triangles with solid line: Ge; diamonds with dotted line: Si (after Nesher et al., Ref. [62]).

from the solutions of which an optical excitation spectrum can be constructed easily. A detailed discussion of the real-space formalism [21] and implementation [22] can be found elsewhere.

Here, we demonstrate the power of this approach by considering a recent computation of *ab initio* absorption spectra and optical gaps for hydrogen-passivated Ge nanocrystals [62] and how they compare to those of Si nanocrystals [63]. One motivation for these calculations was the open question of the presence or absence of a crossover between the optical gaps of Si and Ge nanocrystals. Effective mass theory calculations [64] predicted that below a critical radius Ge nanocrystals would exhibit an optical gap larger than that of Si even though the bulk optical gap of Ge is smaller than that of Si, due to the smaller effective mass of carriers in Ge. Subsequently, tight-binding calculations also found a cross-over [65], albeit at a different critical radius, but empirical pseudopotential calculations did not [66]. Delta self-consistent field “(Δ SCF)” calculations [67] also did not reveal a cross-over, but this method is not rigorously anchored within DFT because of the use of a filled orbital that is not the highest occupied state. Clearly, such a situation called for *ab initio* calculations that do not employ any parameterization and do not require any experimental input.

Figure 9 compares TDDFT results for the optical gap of both Si and Ge nanocrystals with all known previous calculations. Approximately spherical hydrogen-passivated Ge and Si nanocrystals were considered throughout, with the smallest “nanocrystals” being GeH_4 and SiH_4 (which are simply the germane and silane molecules), and the largest nanocrystals being $\text{Ge}_{147}\text{H}_{100}$ and $\text{Si}_{147}\text{H}_{100}$. Clearly, TDDFT did not reveal a crossover between the Si and Ge optical gap curves for any crystallite size: the optical gap order is preserved even for the limiting case of germane and silane, although for small enough crystallites the curves closely track each other. Interestingly, the results appear to be in excellent agreement with previous empirical pseudopotential calculations [66], but differ from the other results. This demonstrates the potential of TDDFT in validating semi-empirical methods, which could then be used for even larger nanocrystals.

3.6 Polarizability and exact exchange calculations

The static polarizability tensor, α_{ij} is defined as

$$\alpha_{ij} = \frac{\partial \mu_i}{\partial F_j}, \quad (12)$$

where i, j correspond to x, y , or z , μ_i is the dipole moment in the i direction and F_j is an external electric field in the j direction. This is an important quantity because it is experimentally accessible and because it often teaches us about less accessible chemical and physical properties of the system [68, 69].

In particular, for nanoclusters it is one of the few readily measurable quantities and comparison with theory can be used for an indirect verification of cluster structures in a manner similar to the photoemission spectra example discussed above [50, 53, 70, 71].

PARSEC offers a simple, by-definition calculation of Eq. (12) because of the use of open boundary conditions. The absence of periodicity allows for the explicit addition of an external electric field term, $-F\hat{r}$, in the Hamiltonian. This, in turn, allows us to use the finite field method [70], where the dipole is computed without an external electric field and then with an external electric field in various directions. The polarizability tensor is then determined by evaluating the partial derivatives in Eq. (12) via a simple numerical derivative. We find this approach to be much easier than the typical sum-over-states perturbation theory approach as the need for obtaining a large number of unoccupied states is avoided entirely. Recently, we have shown that even a numerically much more sensitive quantity such as the second hyperpolarizability γ_{ijkl} , defined as:

$$\gamma_{ijkl} = \frac{\partial^3 \mu_i}{\partial F_j \partial F_k \partial F_l}, \quad (13)$$

can also be reliably obtained using PARSEC. This was achieved simply by using a series of external electrical fields with different magnitude for evaluating the derivatives [72].

Here, we demonstrate this ability of PARSEC by considering the electric field response of hydrogen chains. Before turning to this example, however, a discussion of another new feature of PARSEC is required. In all applications surveyed above, the density functional used was invariably LDA or GGA. While this is clearly sufficient for many material classes, it is not a panacea. A striking example of LDA/GGA failure is that the polarizability and especially the hyperpolarizability of molecular chains such as polyacetylene are drastically over estimated by LDA/GGA [74], whereas a (usually much cruder) Hartree–Fock calculation provided for a reasonable answer. This strongly suggests that the problem lies with the approximate treatment of exchange in LDA/GGA. However, the treatment of exchange exactly within DFT is very difficult. This is because the expression of the exchange energy in terms of *orbitals* rather than charge density significantly complicates the determination of the Kohn–Sham exchange potential. The latter is the functional derivative of the exchange energy with respect to the charge density. Because the exchange energy is now only an implicit functional of the density, an additional, implicit integro-differential equation for determining the exchange potential, known as the optimized effective potential (OEP) equation [27], is required. Determining a sensitive quantity such as the second hyperpolarizability with exact exchange was therefore considered to be too difficult. Instead, approximations such as the Krieger–Li–Iafrate (KLI) [75] or the common energy denominator approximation (CEDA) [76], often regarded as practically equivalent to exact exchange within DFT, were used instead. Surprisingly, these approximations still yielded results inferior to a Hartree–Fock calculation [74, 76].

We have been able to use PARSEC for obtaining the hyperpolarizability of hydrogen chains within exact-exchange DFT without further approximations [73]. This was achieved by a reasonably straightforward implementation of a recently proposed formalism for coupling the Kohn–Sham equation with the OEP equation [77]. Calculating the second hyperpolarizability as outlined above, we reproduced the LDA and KLI results reported previously. We found that, e.g., for a chain of twelve hydrogen atoms the LDA result overestimates the Hartree–Fock one by almost an order of magnitude and that the KLI result still over estimates it by a factor of two. Most importantly, we found that exact exchange within DFT without additional approximations yields a result that is essentially the same as that obtained from Hartree–Fock theory despite the significant differences between the two approaches. Our calculations were also able to determine the cause for the striking differences between the results obtained with the different functionals. Figure 10 shows the difference between the exchange potential with and without external electric field for OEP, KLI, and LDA, for the case of H_8 (a similar picture is obtained for H_{12}). Clearly, the OEP response is opposite to the external field, i.e., it contains a strong field-counteracting term, as expected from the Le Chatelier principle. This field-counteracting property is completely missing in the LDA potential because it can only follow the charge density [74]. It does exist in the KLI result, but is underestimated significantly.

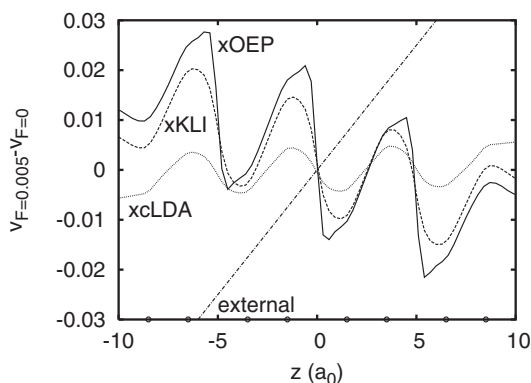


Fig. 10 Potential distributions for a H_8 chain (H atoms are marked by circles on the x -axis): The full line shows the difference between $v_x^{OEP}(0,0,z)$ with an electric field $F = 0.005 e/a_0^2$ and with $F = 0$. Dashed and double-dotted line show the same for v_x^{KLI} and v_x^{LDA} . Straight dash-dotted line shows the potential corresponding to the external electric field F . Note the opposite overall biases of $v_x^{OEP/KLI}$ and v_x^{LDA} (after Kümmel et al., Ref. [73]).

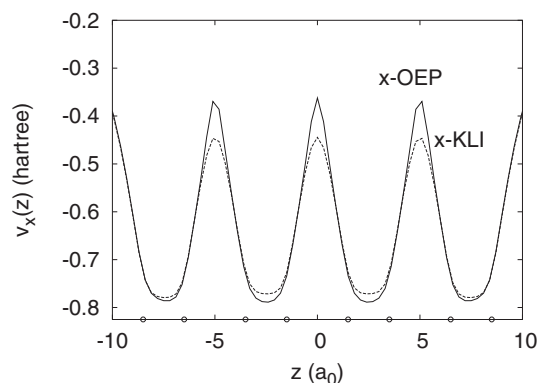


Fig. 11 Potential distributions for a H_8 chain (H atoms are marked by circles on the x -axis): KLI and OEP potentials without an electric field (after Kümmel et al., Ref. [73]).

The cause for the quantitative failure of KLI is immediately apparent if one compares the KLI and OEP exchange potentials in the absence of an electric field, as shown in Fig. 11. While the OEP and KLI results are very similar within each H_2 sub-unit, the OEP calculations lead to considerably higher barriers between the sub-units. For field-free calculations, this is not significant as there's very little charge in the barrier region. However, a change in barrier height will surely affect the capability of the electric field to push the electron distribution from one sub-unit to the other, i.e., change the polarizability and hyperpolarizability. This explains why KLI fails here despite giving a ground state energy that is very similar to that obtained by OEP.

4 Conclusion

In this article, we have explained the essence of our pseudopotential real-space finite difference approach to solving the Kohn–Sham equations, as implemented in PARSEC. We have demonstrated various capabilities of PARSEC, including the usage of open or periodic boundary conditions, spin-polarized calculations, molecular dynamics, linear-response time-dependent DFT, polarizability calculations, and exact exchange calculations using optimized effective potentials. By showing actual usage of PARSEC towards the elucidation of various physical questions, we hope to have showed that PARSEC emerges as a powerful computational tool for a wide range of materials science issues in general and for nano-scale research in particular.

Acknowledgments LK wishes to acknowledge the support of the Israel Science Foundation (under the “Bikura” Program), the Minerva Foundation, the Gerhard Schmidt Minerva Center for supramolecular architecture, the European Union “PHOREMOST” Network of Excellence on nanophotonics, and the Delta Career Development Chair. MMGA acknowledges support from the Spanish Ministry of Education and Science (Program “Ramón y Cajal”), the Spanish Ministry of Education and Science in conjunction with the European Regional Development Fund (Project FIS2005-04239), and the Galician Supercomputer Center (CESGA). JRC would like to acknowledge NERSC and TACC for computer time, as well as NSF (DMR-0551195) and DOE (DE-FG02-03ER25585 and -03ER15491) grants.

References

- [1] P. Hohenberg and W. Kohn, *Phys. Rev.* **136**, B864 (1964).
- [2] W. Kohn and L. J. Sham, *Phys. Rev.* **140**, A1133 (1965).
- [3] R. M. Martin, *Electronic Structure: Basic Theory and Practical Methods* (Cambridge University Press, Cambridge, 2004), chap. 11.
- [4] J. R. Chelikowsky and M. L. Cohen, *Ab initio Pseudopotentials for Semiconductors*, Handbook on Semiconductors (Elsevier, Amsterdam, 1992), Vol. 1, p. 59.
- [5] M. C. Payne, M. P. Teter, D. C. Allen, T. A. Arias, and J. D. Joannopoulos, *Rev. Mod. Phys.* **64**, 1045 (1992).
- [6] W. E. Pickett, *Comp. Phys. Rep.* **9**, 115 (1989).
- [7] M. D. Segall, P. J. D. Lindan, M. J. Probert, C. J. Pickard, P. J. Hasnip, S. J. Clark, and M. C. Payne, *J. Phys.: Condens. Matter* **14**, 2717 (2002).
- [8] G. Kresse and J. Hafner, *J. Phys.: Condens. Matter* **6**, 8245 (1994).
- [9] J. R. Chelikowsky, N. Troullier, and Y. Saad, *Phys. Rev. Lett.* **72**, 1240 (1994).
- [10] A. Stathopoulos, S. Ögüt, Y. Saad, J. R. Chelikowsky, and H. Kim, *Comput. Sci. Eng.* **2**, 19 (2000).
- [11] J. R. Chelikowsky, L. Kronik, I. Vasiliev, M. Jain, and Y. Saad, in: *Handbook of Numerical Analysis*, Vol. 10 (Elsevier, Amsterdam, 2003), pp. 613–637.
- [12] M. M. G. Alemany, M. Jain, J. R. Chelikowsky, and L. Kronik, *Phys. Rev. B* **69**, 075101 (2004).
- [13] A. L. Efros and M. Rosen, *Annu. Rev. Mater. Sci.* **30**, 475 (2000).
- [14] L. Bányai and S. W. Koch, *Semiconductor Quantum Dots* (World Scientific, Singapore, 1993).
- [15] A. D. Yoffe, *Adv. Phys.* **51**, 799 (2002).
- [16] B. Fornberg and D. M. Sloan, in: *Acta Numerica 94*, edited by A. Iserles (Cambridge, Cambridge University Press, 1994).
- [17] D. K. Jordan and D. A. Mazziotti, *J. Chem. Phys.* **120**, 574 (2004).
- [18] N. Troullier and J. L. Martins, *Phys. Rev. B* **43**, 1993 (1991).
- [19] L. Kleinmann and D. M. Bylander, *Phys. Rev. Lett.* **48**, 1425 (1982).
- [20] Y. Saad, *Iterative Methods for Sparse Linear Systems*, 2nd ed. (SIAM, 2003), pp. 187–194.
- [21] I. Vasiliev, S. Ögüt, and J. R. Chelikowsky, *Phys. Rev. B* **65**, 115416 (2002).
- [22] W. R. Burdick, Y. Saad, L. Kronik, I. Vasiliev, M. Jain, and J. R. Chelikowsky, *Comput. Phys. Commun.* **156**, 22 (2003).
- [23] D. M. Ceperley and B. J. Alder, *Phys. Rev. Lett.* **45**, 566 (1980).
- [24] J. P. Perdew, K. Burke, and M. Ernzerhof, *Phys. Rev. Lett.* **77**, 3865 (1996).
- [25] R. van Leeuwen and E. J. Baerends, *Phys. Rev.* **49**, 2421 (1994).
- [26] M. E. Casida and D. R. Salahub, *J. Chem. Phys.* **113**, 8918 (2000).
- [27] T. Grabo, T. Kreibich, and E. K. U. Gross, *Mol. Eng.* **7**, 27 (1997).
- [28] R. B. Morgan and D. S. Scott, *SIAM J. Sci. Stat. Comput.* **7**, 817 (1986).
- [29] R. B. Lehoucq, K. Maschhoff, D. Sorensen, and C. Yang, the ARPACK software package, <http://www.caam.rice.edu/software/ARPACK/>
- [30] See, e.g., R. McWeeny, *Symmetry: An Introduction to Group Theory and Its Applications* (Dover Publications, Mineola, 2002).
- [31] V. Eyert, *J. Comput. Phys.* **124**, 271 (1996).
- [32] Recall that full diagonalization of a dense matrix scales as N^3 , where N is the size of the matrix. Therefore, replacing an eigen-problem of size N by two eigen-problems of size $N/2$ each leads to a four-fold gain in numerical load. For partial diagonalization of sparse matrices, the scaling is lower than N^3 but greater than N , and so there is still significant net gain.
- [33] X. Huang, E. Lindgren, and J. R. Chelikowsky, *Phys. Rev. B* **71**, 165328 (2005).
- [34] Note that the HOMO–LUMO gap computed within time-independent DFT is not expected to be equal to the optical gap, as elaborated in the section on time-dependent DFT below. Nevertheless, often a reasonable description of the unoccupied orbitals is obtained with time-dependent DFT, and the size dependence of the gap does provide for qualitatively correct results. See, e.g., D. V. Melnikov and J. R. Chelikowsky, *Solid State Commun.* **127**, 361 (2003).
- [35] See, e.g., M. L. Cohen and J. R. Chelikowsky, *Electronic Structure and Optical Properties of Semiconductors* (Springer, Berlin, 1988).
- [36] J. R. Chelikowsky, L. Kronik, and I. Vasiliev, *J. Phys.: Condens. Matter* **15**, R1517 (2003).
- [37] J. Ihm, A. Zunger, and M. L. Cohen, *J. Phys. C, Solid State Phys.* **12**, 4409 (1979).

- [38] H. Yu, J. Li, R. A. Loomis, L. W. Wang, and W. E. Buhro, *Nature Mater.* **2**, 517 (2003).
- [39] U. von Barth and L. Hedin, *J. Phys. C: Solid State Phys.* **5**, 1629 (1972).
- [40] A. K. Rajagopal and J. Callaway, *Phys. Rev. B* **7**, 1912 (1973).
- [41] X. Huang, A. Makmal, J. R. Chelikowsky, and L. Kronik, *Phys. Rev. Lett.* **94**, 236801 (2005).
- [42] S. A. Wolf, D. D. Awschalom, R. A. Buhrman, J. M. Daughton, S. V. Molnar, M. L. Roukes, A. Y. Chtchelkanova and D. M. Treger, *Science* **294**, 1488 (2001).
- [43] D. J. Norris, N. Yao, F. T. Charnock, and T. A. Kennedy, *Nano Lett.* **1**, 3 (2001).
- [44] S. Sapra, D. D. Sarma, S. Sanvito, and N. A. Hill, *Nano Lett.* **2**, 605 (2002).
- [45] Y. D. Park, A. T. Hanbicki, S. C. Erwin, C. S. Hellberg, J. M. Sullivan, J. E. Mattson, T. F. Ambrose, A. Wilson, G. Spanos, and B. T. Jonker, *Science* **295**, 651 (2002).
- [46] T. Dietl, H. Ohno, F. Matsukura, J. Cibert, and D. Ferrand, *Science* **287**, 1019 (2000).
- [47] N. Binggeli, J. L. Martins, and J. R. Chelikowsky, *Phys. Rev. Lett.* **68**, 2956 (1992).
- [48] R. N. Barnett and U. Landman, *Phys. Rev. B* **48**, 2081 (1993).
- [49] F. Reif, in: *Statistical and Thermal Physics* (McGraw-Hill, New York, 1965), section 15.5, pp. 560–567.
- [50] L. Kronik, I. Vasiliev, M. Jain, and J. R. Chelikowsky, *J. Chem. Phys.*, **115**, 4322 (2001).
- [50] L. Kronik, I. Vasiliev, and J. R. Chelikowsky, *Phys. Rev. B* **62**, 9992 (2000).
- [51] L. Kronik, R. Fromherz, E. Ko, G. Ganteför, and J. R. Chelikowsky, *Nature Mater.* **1**, 49 (2002); *Eur. J. Phys. D* **24**, 33 (2003).
- [52] S. Li, M. M. G. Alemany, and J. R. Chelikowsky, *Phys. Rev. B* **71**, 165433 (2005).
- [53] N. Binggeli and J. R. Chelikowsky, *Phys. Rev. Lett.* **75**, 493 (1995).
- [54] M. Moseler, B. Huber, H. Häkkinen, U. Landman, G. Wrigge, M. Astruc Hoffmann, and B. v. Issendorff, *Phys. Rev. B* **68**, 165413 (2003).
- [55] O. Guliamov, L. Kronik, and K. A. Jackson, *J. Chem. Phys.* **123**, 204312 (2005).
- [56] K. A. Jackson, M. Horoi, I. Chaudhuri, Th. Frauenheim, and A. A. Shvartsburg, *Phys. Rev. Lett.* **93**, 13401 (2004).
- [57] M. A. Hoffmann, G. Wrigge, B. v. Issendorff, J. Müller, G. Ganteför, and H. Haberland, *Eur. Phys. J. D* **16**, 9 (2001).
- [58] R. M. Dreizler and E. K. U. Gross, *Density Functional Theory* (Springer, Berlin, 1990).
- [59] E. Runge and E. K. U. Gross, *Phys. Rev. Lett.* **52**, 997 (1984).
- [60] See, e.g., M. A. L. Marques and E. K. U. Gross, in: *Primer in Density Functional Theory*, edited by C. Fiolhais, F. Nogueira, and M. A. L. Marques (Springer, Berlin, 2003).
- [61] M. E. Casida, in: *Recent Advances in Density Functional Methods, Part 1*, edited by D. P. Casida (World Scientific, Singapore (1995), p. 155; in: *Recent Developments and Applications of Modern Density Functional Theory*, edited by J. K. Seminario (Elsevier, Amsterdam, 1996), p. 391.
- [62] G. Neshet, L. Kronik, and J. R. Chelikowsky, *Phys. Rev. B* **71**, 35344 (2005).
- [63] I. Vasiliev, S. Ögüt, and J. R. Chelikowsky, *Phys. Rev. Lett.* **86**, 1813 (2001).
- [64] T. Takagahara and K. Takeda, *Phys. Rev. B* **53**, R4205 (1996).
- [65] N. A. Hill, S. Pokrant, and A. J. Hill, *J. Phys. Chem. B* **103**, 3156 (1999).
- [66] F. A. Reboredo and A. Zunger, *Phys. Rev. B* **62**, R2275 (2000).
- [67] H.-Ch. Weissker, J. Furthmüller, and F. Bechstedt, *Phys. Rev. B* **69**, 115310 (2004).
- [68] J. K. Nagle, *J. Am. Chem. Soc.* **112**, 4741 (1990).
- [69] D. Rayane, R. Antoine, P. Dugourd, E. Benichou, A. R. Allouche, M. Aubert-Frecon, and M. Broyer, *Phys. Rev. Lett.* **84**, 1962 (2000).
- [70] I. Vasiliev, S. Ögüt, and J. R. Chelikowsky, *Phys. Rev. Lett.* **78**, 4805 (1997).
- [71] S. Kümmel, J. Akola, and M. Manninen, *Phys. Rev. Lett.* **84**, 3827 (2000).
- [72] S. Kümmel and L. Kronik, *Comput. Mater. Sci.* **35**, 321 (2006).
- [73] S. Kümmel, L. Kronik, and J. P. Perdew, *Phys. Rev. Lett.* **93**, 213002 (2004).
- [74] S. J. A. van Gisbergen, P. R. T. Schipper, O. V. Gritsenko, E. J. Baerends, J. G. Snijders, B. Champagne, and B. Kirtman, *Phys. Rev. Lett.* **83**, 694 (1999).
- [75] J. B. Krieger, Y. Li, and G. J. Iafrate, *Phys. Rev. A* **45**, 101 (1992).
- [76] M. Grüning, O. Gritsenko, and E. Baerends, *J. Chem. Phys.* **116**, 6435 (2002).
- [77] S. Kümmel and J. P. Perdew, *Phys. Rev. B* **68**, 35103 (2003).